

VLA observations of broad 6-cm excited state OH lines in W49A

Patrick Palmer,¹*, W. M. Goss,²†

¹Department of Astronomy and Astrophysics, University of Chicago, 5640 S. Ellis Ave., Chicago, IL 60637

²National Radio Astronomy Observatory, P. O. Box O, Socorro, NM 87801

12 June 2018

ABSTRACT

Using the Very Large Array (VLA), we observed all three of the 6-cm lines of the $^2\Pi_{1/2}, J = 1/2$ state of OH with sub-arcsecond resolution (~ 0.4 arcsec) in W49A. While the spatial distribution and the range in velocities of the 6-cm lines are similar to those of the ground state (18-cm) OH lines, a large fraction of the total emission in all three 6-cm lines has large linewidths ($\sim 5 - 10$ km s $^{-1}$) and is spatially-extended, very unlike typical ground state OH masers which typically are point-like at VLA resolutions and have linewidths ≤ 1 km s $^{-1}$. We find brightness temperatures of 5900 K, 4700 K, and ≥ 730 K for the 4660-MHz, 4750-MHz, and 4765-MHz lines, respectively. We conclude that these are indeed maser lines. However, the gains are ~ 0.3 , again very unlike the 18-cm lines which have gains $\geq 10^4$. We compare the excited state OH emission with that from other molecules observed with comparable angular resolution to estimate physical conditions in the regions emitting the peculiar, low-gain maser lines. We also comment on the relationship with the 18-cm masers.

Key words: masers – ISM:molecules – ISM:individual(W49A) – radio lines:ISM

1 INTRODUCTION

The $^2\Pi_{1/2}, J = 1/2$ rotationally excited state of OH has three hyperfine transitions in the 6-cm band: F=1→0 ($\nu_0 = 4765.562$ MHz), F=1→1 ($\nu_0 = 4750.656$ MHz), and F=0→1 ($\nu_0 = 4660.242$ MHz). Emission from this state of OH was discovered (Zuckerman et al. 1968) and is most frequently observed (Cohen, Masheder & Walker 1991; Cohen, Masheder & Caswell 1995; Dodson & Ellingsen 2002; Smits 2003) as maser emission in the 4765-MHz line. The linewidths are typically < 1 km s $^{-1}$. Another type of emission was detected with linewidths of a few to 20 km s $^{-1}$, first in the 4660-MHz line in Sgr B2 (Gardner, Ribes & Sinclair 1971) and shortly afterward in both the 4750-MHz and 4765-MHz lines as well (Gardner & Ribes 1971). The broad lines had much lower peak flux densities than the narrow 4765-MHz lines which are typically observed to have peak densities exceeding 1 Jy. Subsequently, (Rickard, Zuckerman & Palmer 1975; Rickard, Palmer & Zuckerman 1980; Gardner & Martin-Pintado 1983) observed emission with large line widths in a number of sources including W49A, the subject of this paper. The differences between the two types of emission seemed clearcut: 1) large linewidths vs. narrow linewidths; 2) angular sizes measurable with single dish telescopes vs. point-like sources; and 3) low peak luminosities versus high.

After the detection of analogous broad emission lines from

the $^2\Pi_{3/2}, J = 5/2$ near 5-cm wavelength in Sgr B2, as well as broad absorption features in the 5-cm lines in W3(C), Rickard et al. (1975) suggested that the broad lines (emission and absorption) be called “quasi-thermal”: i.e. close to thermal excitation (which included low gain masers) in contrast to the excitation of strong, high gain masers such as the ground state 18-cm lines, the narrow 4765-MHz lines, and the intense, narrow 5-cm and 2-cm OH masers (Yen et al. 1969; Turner, Palmer & Zuckerman 1970).

The suggestion of Gardner & Martin-Pintado (1983) that both masers and quasi-thermal emission originate in the same clouds, i.e. “that masers are hot spots within an envelope defined by the extent of the quasi-thermal emission” could only be checked by interferometric observations. Guilloteau, Baudry & Walmsley (1985) carried out observations of 4750-MHz emission and 4660-MHz absorption with the VLA which, when combined with 4765-MHz observations of Gardner, Whiteoak & Palmer (1983), showed that this view was plausible for W3(OH). Subsequent interferometric studies (Sgr B2: Gardner, Whiteoak & Palmer 1987; W49A: Palmer, Goss & Whiteoak 2004, hereafter: PGW), showed that while the broad 4660- and 4750-MHz emission regions were smaller than estimated from single dish studies, they were spatially resolved, unlike the narrow linewidth 4765-MHz masers, many of which have angular sizes ~ 5 mas (Palmer, Goss & Devine 2003, hereafter PGD).

Theoretical models to explain emission and absorption in a number of excited state OH lines simultaneously for several sources have included all lines in the analysis (Cesaroni & Walmsley 1991; Jones et al. 1994). However, the 10-20 km s $^{-1}$ wide lines observed in W49A and Sgr B2 have not yet been successfully modelled.

* E-mail: ppalmer@oskar.uchicago.edu

† E-mail: mgoss@nrao.edu

In this study we have observed all three 6-cm excited state OH lines from W49A with the VLA to determine if the broad line sources would break up into small clumps of narrower linewidth features when observed with resolution ≤ 1 arcsec. In addition, we planned to determine the brightness temperatures and to determine precisely, both spatially and in velocity, the relationship between emission in these OH lines and emission and absorption in other molecular lines and the ionized gas. Finally, we address the origins of these broad lines.

2 OBSERVATIONS

The observations were conducted in four sessions using the VLA of the National Radio Astronomy Observatory¹. The bulk of the data reported here are the high angular resolution A- and BnA-configuration observations obtained in 2002. Brief observations with lower angular resolution were conducted in 2001. The pointing positions and centre V_{LSR} 's are provided in Table 1; other parameters of these observations are summarized in Table 2. The distance to W49A is 11.4 kpc (Gwinn, Moran & Reid 1992).

On 2002 April 1, the 4660- and 4750-MHz lines were observed for alternating 20 minute intervals, separated by a 3 minute observation of the phase calibrator at each frequency. This scheme allowed coverage of an hour angle range of about ± 3.5 hours for each line. The bandpass calibrator was observed for 11 minutes at each frequency at the beginning of the session. The 4765-MHz line was observed on 2002 June 1 following an analogous strategy: a 17 minute observation on source was followed by a 3 minute observation of the phase calibrator. However, the hour angle coverage was less extensive (+2.1 hour to +4.4 hours) so that imaging quality is not as favourable for the continuum sources, but is noise-limited for the compact maser regions. The bandpass calibrator was observed for 13 minutes at the end of the session. Both 2001 observations consisted of two scans separated by about an hour and took place at rather large hour angles. The bandpass calibrator used on each date is listed in Table 2. The same phase calibrator was used in all observations (1821+107). The flux density scale was set by observations of 3C286 (April 1 and August 27) or 3C48 (June 1 and November 15).

The correlator setup generated spectra with 127 independent Hanning smoothed channels with widths 12.207 kHz. The velocity resolution differed slightly among the three lines because of the difference in rest frequencies. The velocity resolution is shown in the fourth column of Table 2. The total velocity range covered in these observations was $\sim \pm 40$ km s $^{-1}$.

All data were reduced with the NRAO's AIPS reduction package. For the large datasets obtained in 2002, two sets of images were made. One set was made at the full resolution available in the dataset (corresponding to the synthesised beams provided in the last column of Table 2). In addition, the 4660- and 4750-MHz images (2002 April 1) were convolved to 1-arcsec resolution to improve the signal-to-noise for low brightness emission; the 4765-MHz image (2002 June 1) was convolved to 2-arcsec resolution both to improve the signal-to-noise and to produce a circular beam (in the BnA data, the beam was elongated by about 3:1). The full-resolution images were primarily used to determine properties of small sources; the

convolved images were primarily used to study the relatively low brightness extended OH emission lines.

3 RESULTS

All three of the 6-cm OH lines in W49A are found to have large linewidth, spatially extended components and narrow linewidth, small or point-like components. Fig. 1(a) is an image of the 3.6-cm continuum emission reported by De Pree, Mehringer & Goss (1997) (hereafter DMG). The components discussed in this paper are indicated by a cross and labelled (using the names provided by DMG). The 6-cm OH line sources are observed at a number of positions in central 2 – 3 arcmin in W49A, but the large linewidth, spatially-extended components are observed only in a region about 15×6 arcsec 2 extending E-W over sources G, E, B, and A of DMG. This region is the primary focus of this paper and we will refer to it as the “extended OH region”. Furthermore, even within this small region, most of the line flux density originates from the $\sim 7 \times \sim 5$ arcsec 2 region of source G. A number of small angular size sources were observed in all three lines both within and outside the extended OH region. The extended OH region will be discussed in Section 3.1; the 6-cm OH emission sources outside of this region will be discussed briefly in Section 3.2.

3.1 Extended OH region

The bulk of the emission in all three lines is confined to the source G region. Fig. 1(b) – (d) show the zeroth moment of the 4660-, 4750-, and 4765-MHz OH emission superimposed on the continuum. Both extended and point-like components are observed. While a large fraction of the emission arises from the source G region, emission continues westward across source B in all three lines; in the 4660- and 4765-MHz lines emission continues farther westward across source A. Roughly, the line emission in these regions follows the continuum emission. However, in detail there are numerous differences among the three line images and between each of the line images and the continuum. For example, the 4750-MHz image shows a secondary maximum near source B which is not evident in either the 4660- or the 4765-MHz data. In the full resolution data, while all three lines show a number of point-like sources, the current high spatial resolution data shows that the emission cannot be accounted for by a collection of point-like sources. A significant fraction of the emission in all three lines is spatially extended (see also Section 4.2).

In order to analyse the extended emission at 4660- and 4750-MHz, we used the AIPS program XGAUS to fit single Gaussians at each pixel (RA, Dec) for which three consecutive velocity channels had signals $\geq 3\sigma$. Therefore, XGAUS discriminates against very narrow lines; such lines were located by visual inspection. The fits were done on images convolved to 1-arcsec resolution and the results are displayed in Fig. 3. For each line, the amplitude, V_{LSR} , and FWHM at each pixel are plotted. (In a few small areas there are clearly two components; these were fit separately, but are not displayed.)

3.1.1 Comparison with earlier results

Inspection of Fig. 1(a) – (c) shows that the angular sizes ~ 30 arcsec reported in early single dish studies were a result of beam smearing. Even the smallest single dish beam used [2.6 arcmin (Rickard et al. 1980, hereafter: RPZ)] blended together sources A – G; and, at

¹ The National Radio Astronomy Observatory is a facility of the National Science Foundation operated under cooperative agreement by Associated Universities, Inc.

4660- and 4765-MHz, the 2.6-arcmin beam blended in other OH line emission in the field.

To facilitate comparisons with earlier single dish results, the line profiles integrated over the extended OH region (sources G – A) are presented in Fig. 2. Fig. 2(a) – (c) show the integrated profiles from the high spatial resolution 2002 data, and Fig. 2(d) and (e) display the integrated profiles from the lower spatial resolution 2001 data. In these spatially averaged spectra, only the 4765-MHz spectrum [Fig. 2(c)] contains obvious narrow components at $V_{\text{LSR}} \sim 2.3$ and $\sim 16.0 \text{ km s}^{-1}$. The spectral baseline has a rather large slope in Fig. 2(a) and (b). This slope is due to the missing short spacings in the A-array. The spectral baseline slope in Fig. 2(e) is present because no bandpass calibrator was observed on that date.

The peak flux densities in all three lines from earlier measurements and from this paper are provided in Table 3. Values quoted without error bars were read from plots with poorly determined precision. The VLA spectra were integrated over a box which includes sources G – A and is therefore larger than the synthesised beam. For the VLA observations, the size of the box used is tabulated in the fourth column of Table 3. In the D-array data (2001 Nov 15) a noticeably larger box was used because the synthesised beam was ~ 16 arcsec. The single dish spectra differ in character from the VLA spectra because the single dish beams include varying contributions from sources outside of the extended OH region. Because the VLA spectra are constructed by integrations over many synthesised beams, they are unaffected by emission outside of the extended OH region. This difference is not significant for extended component measurements except at 4765-MHz. Inspection of Table 3 shows that there is no evidence for variability of the broad components — very unlike the behaviour of the narrow components at 4765-MHz (see PGW). In addition, because the flux densities are so similar for the entire range of resolutions, there is no evidence that a significant amount of the flux density is resolved by the A-array (i.e no evidence that there is a component of OH emission with size ≥ 10 arcsec).

3.1.2 4660-MHz

Inspection of Fig. 3(a) reveals OH emission at or near the positions of DMG sources A, B, E, and throughout the G complex. Within this complex, the most intense OH lines arise near G_2 . Fig. 3(c) and (e) show that there is a large velocity gradient across source A and that the FWHM is largest ($\geq 15 \text{ km s}^{-1}$) in the western part of this source. Source B has the most extreme velocity in the region with a smaller FWHM ($\sim 4 \text{ km s}^{-1}$). Source E has an intermediate V_{LSR} and FWHM ($\sim 7 \text{ km s}^{-1}$). Finally, within source G, V_{LSR} and FWHM vary by significant amounts, but lie within the range of values observed in the other sources.

In a spectrum integrated over the source A region at 4660-MHz, two components are separated in velocity by $\sim 10 \text{ km s}^{-1}$ [see Fig. 4(a)]. The presence of two components causes the apparently extreme FWHM for this component in Fig. 3(e). However, fits on a pixel-by-pixel basis in the full resolution data reveal the apparent duplicity to be due to two spatially unresolved components separated by ~ 0.15 arcsec. The position, peak flux density, V_{LSR} , and FWHM of these components are summarised in Table 4.

The spectrum integrated over the source B region is shown in Fig. 4(b). At some velocities there are two components, separated by ~ 0.8 arcsec. The velocities differ by $\sim 0.2 \text{ km s}^{-1}$. However, unlike source A, both components are spatially resolved with sizes ~ 0.5 arcsec. However, because of low signal-to-noise, the two

components are treated as a single entity in further fits. The position, tabulated in Table 4, and an angular size ~ 1 arcsec were determined from a Gaussian fit to the relevant portion of Fig. 3(a). The velocity and FWHM in Table 4 are averages of the central pixels of Fig. 3(c) and (e). The spectrum integrated over source E is shown in Fig. 4(c). Because its peak flux density is only $\sim 10 \text{ mJy}$ and because it is not well resolved from sources B and G, parameters are not tabulated.

The V_{LSR} and FWHM in source G are displayed in Fig. 5(a) and (b). Both quantities vary across the source. The linewidth ranges from $\sim 2 \text{ km s}^{-1}$ to $\sim 20 \text{ km s}^{-1}$. V_{LSR} ranges from $\sim 2 \text{ km s}^{-1}$ to $\sim 8 \text{ km s}^{-1}$. Fig. 6(a) shows the spectrum integrated over the whole of source G; Fig. 6(b) – (f) are the spectra integrated over small regions (0.75 arcsec square) at the positions of sources G_1 – G_5 . Note that all of these spectra are well resolved in velocity with FWHM's ranging from $\sim 6 \text{ km s}^{-1}$ to $\sim 15 \text{ km s}^{-1}$. Because we will compare the OH emission from the source G region with emission and absorption from other molecules, we tabulate the peak flux density, V_{LSR} , and FWHM in Table 5 below. These values were determined from the profile shown Fig. 6(a).

3.1.3 4750-MHz

Fig. 3(b) shows that the 4750-MHz emission has maxima at sources B, E, and at several points in the G region. Source A is not detected at 4750-MHz. The 4660-MHz and 4750-MHz velocity distributions [Fig. 3(c) and (d)] are similar. However, in a band running between sources G_2 and G_3 through source G_4 , the 4750-MHz line is noticeably broader with FWHM as large as $\sim 18 \text{ km s}^{-1}$ [compare Fig. 3(e) and (f)].

The spectrum integrated over the source B region is shown in Fig. 4(d). Due to less favourable signal-to-noise at 4750-MHz, it is not possible to separate spatial components as was done for 4660-MHz. The position listed in Table 4 was derived from a Gaussian fit to the source B region of Fig. 3(b). The velocity and FWHM are averages of the central pixels of Fig. 3(d) and (f). Unlike the 4660-MHz emission from this source, there is no evidence for double lines, and no significant velocity gradient is observed.

At 4750-MHz, emission from source E is more intense and more spatially distinct from B and G than at 4660-MHz. The spectrum integrated over source E is shown in Fig. 4(e). Line parameters and positional information are derived as for source B and tabulated in Table 4.

As at 4660-MHz, the 4750-MHz emission in the source G region is quite complex. The V_{LSR} and FWHM are displayed in Fig. 5(c) and (d). The ranges of V_{LSR} and FWHM are similar to the ranges observed at 4660-MHz. Fig. 7(a) shows a spectrum integrated over source G; Fig. 7(b) – (f) show spectra in the directions of the five DMG components (integrated over boxes at the same positions and having the same sizes as used at 4660-MHz). Compared with similar profiles at 4660-MHz (Fig. 6), small but significant differences are observed. As at 4660-MHz in this region, all of these spectra are resolved in velocity with FWHM's ranging from $\sim 5 \text{ km s}^{-1}$ to $\sim 17 \text{ km s}^{-1}$. Parameters of the line profile integrated over source G [Fig. 7(a)] are presented in Table 5.

3.1.4 4765-MHz

Fig. 1(d) shows the integrated 4765-MHz emission from the extended OH region. The distribution of 4765-MHz emission is similar to the 4660-MHz and 4750-MHz distributions [Fig. 1(b) and

(c)]. The 4765-MHz image has poorer angular resolution (2 arcsec compared with 1 arcsec). Also, at 4765-MHz, there are some unresolved velocity components ($\text{FWHM} \lesssim 1 \text{ km s}^{-1}$) which are bright enough to significantly affect the integrated flux. In particular, the unresolved velocity feature from the source G_4 region [near $V_{\text{LSR}}=2.3 \text{ km s}^{-1}$ in Fig. 2(c)] is the cause of the northward bulge of the contours near this position in Fig. 1(d).

At 4765-MHz, source A is dominated by a single feature with $\text{FWHM} \lesssim 1 \text{ km s}^{-1}$ [see Fig. 4(f)]. Emission from source B at this frequency is less intense (flux density $\sim 10 \text{ mJy/beam}$) than the emission at 4660-MHz and 4750-MHz [compare Fig. 4(b), (d), and (g)]. The position listed in Table 4 and an angular size of $\sim 2 \text{ arcsec}$ were determined from Gaussian fits. Although the values of V_{LSR} are slightly different, all three lines from source B have comparable linewidths (see Table 4).

An analysis of source G at 4765-MHz is similar to the analysis for 4660-MHz and 4750-MHz; Gaussian fitting was not possible due to the inferior angular resolution and unresolved (in velocity) bright components. However, it is apparent that the distribution is complex, and that there are both point-like components and components that are resolved both spatially and in velocity. The spectrum for the whole source G region is shown in Fig. 8(a). Spectra from near the directions of components G_1 and G_4 exhibit narrow features ($\text{FWHM} \lesssim 1 \text{ km s}^{-1}$); see Fig. 8(b) and (c). Parameter values for the sources near G_1 and G_4 are presented in Table 4. Only for G_4 do Gaussian fits yield an non-zero angular size: $\sim 0.3 \text{ arcsec}$.

To determine the line parameters for the extended emission in source G, a Gaussian representing the narrow 2.3 km s^{-1} feature apparent in Fig. 8(a) was initially subtracted. The peak, V_{LSR} , and FWHM of the residual are presented in Table 5.

3.2 Other 6-cm compact OH sources in the W49A region

In addition to the sources discussed above in the $15 \times 6 \text{ arcsec}^2$ region near source G, a number of other OH sources in W49A were detected. The positions, peak flux densities, V_{LSR} 's, and FWHM 's are summarised in Table 4. In most cases, the absolute position error is dominated by calibration uncertainties ($\sim 0.1''$). Most of the sources in Table 4 are unresolved with upper limits in the range $0.4 - 1.0 \text{ arcsec}$, depending on the strength of the OH emission. Exceptions are two sources discussed above (B and G_4) and South 1.

South 1 is a rather unusual 4660-MHz maser. With the velocity resolution used by PGW, this source appeared to be single with angular size $< 1.2 \text{ arcsec}$. At the epoch of this study, and with the present 0.78 km s^{-1} resolution, two components with velocities differing by 4.7 km s^{-1} and separated by 1.0 arcsec are observed. The component with $V_{\text{LSR}}=13.6 \text{ km s}^{-1}$ appears not to have changed, but the component with $V_{\text{LSR}}=18.3 \text{ km s}^{-1}$ was not present in 1984. Both components appear to be spatially resolved in the current study. A critical question we cannot address with the currently available data is whether, if observed with better velocity resolution, each will turn out to be a cluster of point-like components, similar to 4765-MHz masers in W3(OH) and DR21EX (see PGD).

In all three lines, there is emission within a few arcseconds of J_1 , J_2 , and the bright arc associated with the extended source L [see Fig. 1(a) – (c)]. Emission in the individual lines is not coincident; and, except for 4660-MHz, the emission is displaced by $\sim 1 - 3 \text{ arcsec}$ from the continuum sources.

4 DISCUSSION

The broad OH lines ($\text{FWHM} \gtrsim 5 \text{ km s}^{-1}$) have been detected in the directions of sources B and G in all three OH lines (see Fig. 1). Source G is the primary spatially extended source with a linear extent of $\sim 0.3 \text{ pc}$ ($\sim 5 \text{ arcsec}$). Below, we first establish the line of sight location of the OH emitting gas and estimate the physical conditions in the molecular gas. Then, we address the brightness temperatures of the broad lines and show that they are in fact masers; thus population inversions must occur over a $\sim 0.3 \text{ pc}$ region in contrast to the narrow 4765-MHz lines studied by PGD which are confined to AU-scale regions. Finally, we find a striking relationship between the broad 6-cm OH lines and the 18-cm OH emission lines.

4.1 Non-maser molecular line and recombination line studies

Many molecular line studies of W49A have been carried out in the past 30 years. Typically, molecules in this region emit or absorb in two velocity ranges: $\sim 4 \text{ km s}^{-1}$ and $\sim 14 \text{ km s}^{-1}$. However, most of the previous studies do not have sufficient angular resolution to investigate in detail the source A, B, and G region of interest ($15 \times 6 \text{ arcsec}^2$). The high resolution studies of H_2CO (Dickel & Goss 1990), CS (Serabyn, Güsten & Schultz 1993; Dickel et al. 1999), and CH_3CN (Wilner et al. 2001) are valuable for determining the line of sight location of the OH emitting gas with respect to the continuum sources and for estimates of molecular density, projected density, and neutral gas kinetic temperature.

Dickel & Goss (1990) observed 2- and 6-cm H_2CO absorption in W49A with ~ 1.5 -arcsec resolution. Toward source G, H_2CO absorption occurred in three broad, blended features. While H_2CO can absorb the cosmic microwave background, the absorption is so deep that the H_2CO must lie in front of source G. The parameters of the 4.4 km s^{-1} H_2CO feature are similar to those of the 6-cm OH emission (see Table 5). Therefore, the molecular gas in the velocity range in which OH emits lies in front of the HII regions. Toward sources A and B, H_2CO absorption is observed in more restricted velocity ranges. Again, the velocity ranges and line widths agree well with those of the broad OH emission lines. Dickel & Goss (1990) derived a density of $n_{\text{H}_2}=4 \times 10^5 \text{ cm}^{-3}$ (for a temperature 40 K). These authors point out that the 18-cm OH maser velocities are in the range $2 - 8 \text{ km s}^{-1}$. Thus, the ground state maser velocities fall within the velocity extent of the 6-cm OH emission profiles toward source G [see Fig. 6(a), Fig. 7(a), Fig. 8(a)].

Serabyn et al. (1993) carried out a multi-transition study of CS and C^{34}S ($J=3 \rightarrow 2$, $5 \rightarrow 4$, and $7 \rightarrow 6$) in a $\sim 45 \times 24 \text{ arcsec}^2$ region centred on source G. The angular resolution ranged from 12 to 20 arcsec, depending on the transition. Three clumps were identified. The central and the southwest clumps (CS-C and CS-SW) were centred near source G and sources A/B, respectively. For CS-C, V_{LSR} and the FWHM were similar to the corresponding values for 6-cm OH lines integrated over source G listed in Table 5; for CS-SW, V_{LSR} and the FWHM were similar to the corresponding values for 6-cm OH emission from regions A and B listed in Table 4. For an assumed $T_k=50 \text{ K}$, Serabyn et al. (1993) find $n_{\text{H}_2} \sim 10^6 \text{ cm}^{-3}$ and $N_{\text{H}_2} \sim 10^{24} \text{ cm}^{-2}$.

Dickel et al. (1999) report a study of the CS $J=2 \rightarrow 1$ line in W49A with the BIMA array with angular resolution $\sim 4 \text{ arcsec}$. This study has better angular resolution than the Serabyn et al. (1993) study; however, because it involves a lower-lying transition, interpretation is complicated by possible self-absorption. The CS $J=2 \rightarrow 1$ line toward source G shows absorption at $V_{\text{LSR}} \sim 15$

km s^{-1} and emission at $\sim 4 \text{ km s}^{-1}$. The brightness temperature of the background HII region is 17 K at 6-cm. Because the 4 km s^{-1} gas is in front of the HII region (see above), we interpret this observation to show that the kinetic temperature of the gas emitting the 6-cm OH lines toward source G is significantly greater than 17 K. Dickel et al. (1999) also report observations of the C^{34}S $J=3\rightarrow 2$ line with the IRAM telescope. They observed that toward source G the $V_{\text{LSR}}=4 \text{ km s}^{-1}$ component was about 50 per cent of the intensity the 12 km s^{-1} component, while Serabyn et al. (1993) observed these components of the corresponding $J=5\rightarrow 4$ line to have comparable intensity. Dickel et al. (1999) suggested that the differing intensity ratios is evidence for opacity effects in C^{34}S ; however, it might also be further evidence for a higher temperature in the 4 km s^{-1} cloud.

Wilner et al. (2001) observed the $J=12\rightarrow 11$ lines of CH_3CN with the BIMA array with angular resolution ~ 0.8 arcsec. These lines require kinetic temperatures ≥ 50 K. These highly excited lines are found in six discrete regions, including one displaced by 0.6 arcsec from G_1 ($V_{\text{LSR}}=0.9\pm 2 \text{ km s}^{-1}$) and another ~ 0.9 arcsec south of G_2 ($V_{\text{LSR}}=3.7\pm 2 \text{ km s}^{-1}$), while extended emission at a lower level is reported around the B and G regions.

In summary, the high resolution observations of H_2CO , CS, and CH_3CN show that the kinetic temperature of the molecular gas associated with source G is ≥ 50 K, that the density of H_2 is $\sim 10^6 \text{ cm}^{-3}$, and that the column density of H_2 is $\sim 10^{24} \text{ cm}^{-2}$. These values are comparable to those derived from the observations of the 6-cm OH lines (see Section 4.2 and PGD).

Table 6 is a comparison of the positions and velocities of the the excited OH sources with those of the DMG HII regions. The separation between OH sources and DMG continuum components ($\Delta\theta$) are listed. The positional comparisons in Table 6 quantify the visual impression from the moment images in Fig. 1(b) – (d): OH emission in all three lines closely, but imperfectly, follows the continuum emission. In most cases, the displacements of the OH line from the continuum positions are less than the sizes of the continuum components. The three exceptions are: 1) 4750-MHz near source J_2 which as noted above may be associated with the more diffuse source L; 2) South 1, in which the OH position falls on extended emission from the HII complex [see Fig. 1(b) of DMG]; and, 3) source R in which the OH position is displaced from all continuum components [see Fig. 1(f) of DMG].

It is striking that velocities of the 6-cm OH lines do not agree with those of the HII regions. For source G, the OH line velocities are less positive than those of the ionized gas. If the OH is on the near side of the HII complex (as argued above and as expected if the radiation being amplified arises from the HII regions), the molecular gas is flowing away from the HII region toward the observer.

4.2 Brightness temperatures

To determine a lower limit for the brightness temperatures of the 6-cm OH lines, the flux density maxima within source G region were located in the full resolution images. The maximum at 4660-MHz is ~ 0.4 arcsec east of G_2 ; that at 4750-MHz is ~ 0.7 arcsec south of G_5 . Table 7 provides the maximum flux densities and the line brightness temperatures. With a larger synthesised beam, PGW determined lower limits of 1200 K at 4660-MHz and 700 K at 4750-MHz. Were the lines spatially unresolved in both studies, the brightness temperature lower limits would have increased by the ratio of the beam areas, a factor of ~ 40 . Because the increase was only a factor ~ 5 , we conclude that the broad 4660- and 4750-MHz lines from the source G region are spatially resolved in the

current study. Therefore, the values in Table 7 are estimates of the brightness temperatures and not lower limits.

At 4765-MHz, the maximum of the broad component cannot be precisely identified because of the larger synthesised beam and the presence of an intense narrow line near source G_2 . Also we have no earlier VLA data with which to make comparisons. In regions displaced from the narrow components, the lower limit for the brightness temperature exceeds 700 K (see Table 7).

The line brightness temperatures in all three lines are so large that we assume that the populations are inverted and that these are in fact maser lines.

Based on the studies discussed in Section 4.1, and based on the close resemblance of the OH emission distributions with the continuum emission (see Section 3.1), we assume that the OH molecules amplify the continuum emission from the HII regions. For the 4660- and 4750-MHz lines we can make detailed estimates of peak optical depths in the lines and projected densities of OH and H_2 . The continuum brightness temperatures (extrapolated from the 8-GHz data of DMG) at the corresponding points are provided in the fourth column of Table 7. The fifth column provides the OH line peak optical depths. These values are calculated assuming that the excitation temperatures are small compared to the continuum brightness. Although these are maser lines, the gain is small, unlike that in the narrow 4765-MHz lines (see for example, PGD where gains corresponding to $\tau_0 \sim 20$ are observed).

To estimate the projected density of OH required to provide this gain, we follow PGD³. For the broad lines, we use the linewidth 4 km s^{-1} (the smallest values in the region). We estimate that the inversion efficiency lies in the range 0.01 – 0.1, and that the fraction of OH molecules in the $^2\Pi_{1/2}, J = 1/2$ state is in the range 0.03 – 0.1 (corresponding to rotational excitation temperatures 50 – 200 K). For the peak optical depths of the 4660- and 4765-MHz lines, we obtain:

$$\tau_0 = 3.5 \cdot 10^{-17} N_{\text{OH}}; \quad (1)$$

and, for the 4750-MHz line:

$$\tau_0 = 7.0 \cdot 10^{-17} N_{\text{OH}}. \quad (2)$$

The abundance of OH relative to H_2 is uncertain. A number of determinations for relatively diffuse clouds obtain $\frac{n_{\text{OH}}}{n_{\text{H}_2}} \sim 10^{-8}$ (e.g. Crutcher 1979; Liszt & Lucas 1996). For more opaque clouds, values a factor of 10 larger are obtained (e.g. Jones et al. 1994; Harju, Winnberg & Wouterloot 2000). For strong masers, values 10 – 100 times larger are usually invoked (e.g. Pavlakis & Kylafis 1996 and references therein). Because the clouds from which we observe the broad OH lines most resemble the opaque clouds, we adopt a value of $\frac{n_{\text{OH}}}{n_{\text{H}_2}} = 2 \times 10^{-7}$. Finally, we write equations (1) and (2) in terms of N_{H_2} . For the 4660- and 4765-MHz lines:

³ Note that equation (1) of PGD is incorrect. It should read:

$$\tau_0 = \sqrt{\frac{4\ln(2)}{\pi}} \frac{c^2}{8\pi\nu^2} \frac{g_u A_{ul}}{\Delta\nu} \Delta n L.$$

Therefore the coefficients of equations(3) and (5)–(7) should be increased by a factor of 9. Finally, the un-numbered equation following from equation(7) should read

$$L_{AU} = \frac{2 \cdot 10^8}{n_{\text{H}_2}}.$$

The required density in the next sentence should read $n_{\text{H}_2} \geq 2 \cdot 10^5 \text{ cm}^{-3}$.

$$\tau_0 = 7.0 \cdot 10^{-25} N_{H_2}, \quad (3)$$

and for the 4750-MHz line:

$$\tau_0 = 1.4 \cdot 10^{-24} N_{H_2}. \quad (4)$$

The column densities of H₂ required to account for the gains in the fifth column of Table 7 are provided in the final column. These column densities are similar to those derived in the CS study by Serabyn et al. (1993).

Finally, we investigate the consequences of assuming that the OH is on the far side of the HII regions. The background temperature would be ~ 10 K, leading to optical depths of ~ 6.2 which would require an increase of OH column density and therefore H₂ column density by a factor ~ 15 . Unfortunately such an increased column density cannot be ruled out because of the uncertainty in $\frac{n_{OH}}{n_{H_2}}$. Therefore our conclusion that the OH observed is on the near side of the HII regions rests on 1) the H₂CO absorption data, and 2) on the similar shapes of the OH emission distribution and the continuum emission.

4.3 Relationship with 18-cm OH masers

Several authors have studied maser lines from ground state (18-cm) OH and from H₂O in W49A with milli-arcsecond resolution. Many OH masers in all four ground state lines have been discovered near source G (e.g. Gaume & Mutel 1987). A five epoch proper motion study of H₂O masers established that the dynamical centre of an exceptionally powerful outflow is located in source G (Gwinn et al. 1992; De Pree et al. 2000; Wilner et al. 2001). The resolutions of these 18-cm OH and H₂O studies correspond to AU linear scales which are too small to use for determining physical conditions in the extended molecular gas (~ 0.1 pc scales).

Gaume & Mutel (1987) catalogued 367 18-cm OH masers in this region. Fig. 10(a) shows the locations of the masers spots in all four transitions superimposed on the 4660-MHz OH first moment image and the continuum distribution. There are prominent similarities and differences between the distribution of 4660-MHz emission and the 18-cm maser spots. For sources A and B, the 18-cm OH and the 4660-MHz emission are similar. However, for source G, the 18-cm maser spots tend to follow the outer edge of the 4660-MHz distribution (and of the continuum distribution). The phenomenon that 18-cm OH masers associated with compact HII regions tend to fall on the edges of the HII regions is well known (see e.g., Gaume & Mutel 1987). One possible explanation is that the masers are located in molecular gas which is located on the far side of the HII region. Because compact HII regions are optically thick at 18-cm, such masers would be attenuated and not detected. In this view, the concentration at the edges is only apparent due to obscuration of others behind the HII region. However, if this were the correct explanation for the difference in distributions, we would expect that in about 50 per cent of the cases the molecular gas containing the masers would be on the near side of the HII region. Such masers would appear to be distributed across the face of the HII region, and these cases are uncommon. The second explanation is based an expanding spherical HII region. At the edges, lines of sight passing through the sphere have maximum path-lengths in which OH has similar physical conditions and in which the velocity coherence is most favourable. An objection to this explanation is that turbulence in a region of massive star formation may be so large that an organized, spherical outflow is not realized.

Fig. 10(b) is a histogram of the velocities of the 348 18-cm masers in the direction of source G. The maser velocities are

Table 5. Parameters of broad 6-cm OH lines from source G region. The 1- σ uncertainties are listed.

Line (MHz)	S _{max} (mJy)	V _{LSR} (km s ⁻¹)	FWHM (km s ⁻¹)
4660	310(12)	3.8(3)	9.0(8)
4750	270(10)	3.1(3)	6.9(8)
4765	140(9)	4.2(4)	10.2(8)

grouped into bins 1.5 km s⁻¹ wide, and the number per velocity interval is plotted. This plot represents the velocity field in the gas emitting the 18-cm lines independently of the the intensity of the individual features. A simple count of masers unweighted by intensity is of most interest because the high gain 18-cm masers depend on physical conditions at the size scale of the maser spots; such small regions will be unimportant in the formation of the spatially extended broad 6-cm lines. The shape of this distribution is similar to the line shapes of the broad 6-cm lines [compare with Fig. 2(a) – (c)]. Thus, the velocity distribution of the gas emitting the 18-cm masers is similar to that of the gas emitting the broad 6-cm lines as well as the CS lines (see Fig. 7 of Serabyn et al. 1993). The ionized gas and the molecular gas do not have the same average velocity (see Section 4.2) and the gas emitting 18-cm lines and that emitting the 4660-MHz line are in separate regions [as shown by Fig. 10(a)]. Therefore, the similarity of the velocity distributions is surprising, unless all of molecular gas is part of an organized outflow.

4.4 Conclusions

We have presented observations of the broad 6-cm OH lines. These lines are maser lines with linear extents and velocity distributions comparable to the those of several non-maser molecules in this region. However, the low gain, broad 6-cm masers have the same velocity distribution as the high gain 18-cm masers. This similarity suggests that all of the observed OH masers are part of the same outflow from source G, although the broad 6-cm and the 18-cm masers must be located in distinct regions of the outflow.

Several outstanding problems remain. First, an explanation must be found for the excitation of the broad, low gain masers throughout the ~ 0.3 pc diameter region. Second, an explanation must be offered for why we observe that only a small fraction of the total area from which the broad lines arise contains spots with large gains in the 4765-MHz and in the 18-cm lines. In order to resolve the second problem, we suggest that long lines of sight through the turbulent molecular gas may be likely along which the velocity is coherent to within an observed linewidth. New models of turbulent gas in regions of massive star formation are required which provide estimates of the number of such lines of sight that will be expected in a given area at one time, and further provide estimates of how long these coherent lines of sight will exist.

5 ACKNOWLEDGMENTS

P. Palmer thanks the NRAO for hospitality during several extensive visits while this work was carried out.

REFERENCES

Cesaroni, R., Walmsley, C. M. 1991, A&A, 241, 537

Table 1. Pointing positions and central V_{LSR} .

Year	Pointing Position			Central V_{LSR} (km s $^{-1}$)	
	B1950.0	J2000.0			
2001	19 ^h 07 ^m 47 ^s .319	09 ⁰⁰ 00 ⁰ 20 ⁰ .53	19 ^h 10 ^m 10 ^s .948	09 ⁰⁵ 17 ⁰ 67	+8.23
2002	19 ^h 07 ^m 49 ^s .500	09 ⁰¹ 15 ⁰ 00	19 ^h 10 ^m 13 ^s .112	09 ⁰⁶ 12 ⁰ 29	+5.0

Table 2. Observing parameters.

Date	Line (MHz)	Array	ΔV (km s $^{-1}$)	Bandpass Calibrator	Time on Source	RMS (mJy/bm)	Synth. Beam (arcsec x arcsec, PA $^{(0)}$)
2001 Aug 27	4660	C	0.785	3C286	38 min	3.5	6.6 x 4.4, -53
2001 Nov 15	4750	D	0.770	—	35 min	3.9	19. x 14., 56
2002 Apr 01	4660	A	0.785	3C286	169 min	1.4	0.44 x 0.42, -90
2002 Apr 01	4750	A	0.770	3C286	166 min	1.3	0.43 x 0.52, 76
2002 Jun 01	4765	BnA	0.768	3C84	78 min	2.1	1.8 x 0.52, 60

Table 7. Brightness temperatures for broad 6-cm OH components

Line (MHz)	S_{max} (mJy/bm)	T_b (K)	$T_c(m)$ (K)	τ_0	N_{H_2} (cm $^{-2}$)
4660	20	5900	12800	-0.38	5.4 10 23
4750	15	4700	7400	-0.49	3.5 10 23
4765	~15	≥ 730	—	—	—

Cohen, R. J., Masheder, M. R. W., Walker, R. N. F. 1991, MNRAS, 250, 611 (CMW)
Cohen, R. J., Masheder, M. R. W., Caswell, J. L. 1995, MNRAS, 274, 808
Crutcher, R. M. 1979, ApJ, 234, 881
De Pree, C. G., Mehringer, D. M., Goss, W. M. 1997, ApJ, 482, 307 (DMG)
De Pree, C. G., Wilner, D. J., Goss, W. M., Welch, W. J., McGrath, E. 2000, ApJ, 540, 308
Dickel, H. R., Goss, W. M. 1990, ApJ, 351, 189
Dickel, H. R., Williams, J. A., Upham, D. E., Welch, W. J., Wright, M. C. H., Wilson, T. L., Mauersberger, R. 1999, ApJS, 125, 413
Dodson, R. G., Ellingsen, S. P. 2002, MNRAS, 333, 307
Gardner, F. F., Martin-Pintado, J. 1983 A&A, 121, 265 (GM)
Gardner, F. F., Ribes, J. C. 1971, Astophys Lett, 9, 175
Gardner, F. F., Ribes, J. C., Sinclair, M. W. 1971, ApJ, 169, L109
Gardner, F. F., Whiteoak, J. B., Palmer, P. 1983, MNRAS, 205, 297
Gardner, F. F., Whiteoak, J. B., Palmer, P. 1987, MNRAS, 225, 469
Gaume, R. A., & Mutel, R. G. 1987, ApJS, 65, 193
Guilloteau, S., Baudry, A., Walmsley, C. M. 1985, A&A, 153, 179
Gwinn, C. R., Moran, J. M., Reid, M. J. 1992, ApJ, 393, 149
Harju, J., Winnberg, A., Wouterloot, J. G. A. 2000, A&A, 353, 1065
Jones, K. N., Field, D., Gray, M. D., Walker, R. N. F. 1994, A&A, 288, 581
Liszt, H., Lucas, R. 1996, A&A, 314, 917
Palmer, P., Goss, W. M., Devine, K. E. 2003, ApJ, 599, 324 (PGD)
Palmer, P., Goss, W. M., Whiteoak, J. B. 2004, MNRAS, 347, 1164 (PGW)
Pavlakis, K. G., Kylafis, N. D. 1996, ApJ, 467, 300

Rickard, L. J., Palmer, P., Zuckerman, B. 1980, (unpublished manuscript) (RPZ)
Rickard, L. J., Zuckerman, B., Palmer, P. 1975, ApJ, 200, 6
Serabyn, E., Güsten, R., Schultz, A. 1993, ApJ, 413, 571
Smits, D. P. 2003, MNRAS, 339, 1
Turner, B. E., Palmer, P., Zuckerman, B. 1970, ApJ, 160, L125
Yen, J. L., Zuckerman, B., Palmer, P., Penfield, H. 1969, ApJ, 156, L27
Wilner, D. J., De Pree, C. G., Welch, W. J., Goss, W. M. 2001, ApJ, 550, L81
Zuckerman, B., Palmer, P., Penfield, H., Lilley, A. E. 1968, ApJ, 153, L69

Table 3. Peak observed flux densities of the broad 6-cm OH lines in W49A. Estimated uncertainties are listed.

Observers	Date	Instrument	Beamwidth (arcsec)	4660-MHz (mJy)	4750-MHz (mJy)	4765 MHz (mJy)
RPZ	1974 February	Effelsberg	156	300	350	200
GM	1982 February/May	Effelsberg	~180	380(20)	340(20)	0.20(2)
PGW	1984 March	VLA	25.5 x12	400(20)	320(20)	—
CMW	1989 July	Lovell	216	400	300	200
Smits	1994 October/November	Harebeesthoek	600	≤ 1800	≤ 900	—
(this paper)	2001 August 27	VLA	22.8 x15.6	380(40)	—	—
(this paper)	2001 November 15	VLA	40.5 x31.5	—	410(40)	—
(this paper)	2002 April 1	VLA	15 x6	350(40)	300(30)	—
(this paper)	2002 June 1	VLA	15 x6	—	—	190(30)

Table 4. Parameters for compact OH Sources. The $1-\sigma$ uncertainties are listed for the peak flux density, V_{LSR} , and FWHM. For estimated uncertainties in positions, see text.

Nearest DMG Source	Line (MHz)	α (J2000.0)	δ (J2000.0)	Peak (mJy/beam)	V_{LSR} (km s $^{-1}$)	FWHM (km s $^{-1}$)
A	4660	19 ^h 10 ^m 12 ^s .89	09 ⁰⁶ '11"9	30(3)	10.1(3)	7.3(8)
A	4660	19 ^h 10 ^m 12 ^s .90	09 ⁰⁶ '12"0	70(4)	-0.9(1)	4.3(3)
A	4765	19 ^h 10 ^m 12 ^s .89	09 ⁰⁶ '12"1	64(3)	16.3(3)	≤ 1.0
B	4660	19 ^h 10 ^m 13 ^s .17	09 ⁰⁶ '12"7	55(6)	15.2(2)	4.1(5)
B	4750	19 ^h 10 ^m 13 ^s .14	09 ⁰⁶ '12"7	18(4)	13.1(2)	7.4(3)
B	4765	19 ^h 10 ^m 13 ^s .16	09 ⁰⁶ '13"1	10(2)	12.4(2)	6.2(5)
E	4750	19 ^h 10 ^m 13 ^s .25	09 ⁰⁶ '12"4	15(4)	6.1(3)	8.3(3)
G ₁	4765	19 ^h 10 ^m 13 ^s .36	09 ⁰⁶ '12"7	12(3)	-8.0(3)	≤ 1.0
G ₄	4765	19 ^h 10 ^m 13 ^s .52	09 ⁰⁶ '13"9	264(3)	2.3(3)	≤ 1.0
H	4765	19 ^h 10 ^m 13 ^s .63	09 ⁰⁶ '17"8	24(3)	10.7(4)	≤ 1.0
J ₁	4660	19 ^h 10 ^m 14 ^s .14	09 ⁰⁶ '25"2	16(3)	7.4(2)	2.0(10)
J ₂	4750	19 ^h 10 ^m 14 ^s .32	09 ⁰⁶ '22"4	55(2)	4.2(4)	≤ 1.0
J ₂	4765	19 ^h 10 ^m 14 ^s .13	09 ⁰⁶ '27"6	34(2)	7.5(3)	≤ 1.0
O	4765	19 ^h 10 ^m 16 ^s .36	09 ⁰⁶ '06"6	16(2)	-1.5(4)	5.8(10)
R	4765	19 ^h 10 ^m 10 ^s .94	09 ⁰⁵ '17"6	77(2)	11.9(3)	≤ 1.0
South 1	4660	19 ^h 10 ^m 21 ^s .68	09 ⁰⁵ '01"0	70(2)	13.6(3)	≤ 1.5
South 1	4660	19 ^h 10 ^m 21 ^s .68	09 ⁰⁵ '02"1	51(2)	18.3(3)	≤ 1.0

Table 6. Comparison of V_{LSR} : 6-cm OH vs. the ionized gas.

Nearest DMG Source	4660-MHz V_{LSR} (km s $^{-1}$)	4750-MHz V_{LSR} (km s $^{-1}$)	4765-MHz V_{LSR} (km s $^{-1}$)	H92 α V_{LSR} (km s $^{-1}$)	H66 α V_{LSR} (km s $^{-1}$)	H52 α V_{LSR} (km s $^{-1}$)			
	$\Delta\theta$ (arcsec)	$\Delta\theta$ (arcsec)	$\Delta\theta$ (arcsec)	$\Delta\theta$ (arcsec)	$\Delta\theta$ (arcsec)	$\Delta\theta$ (arcsec)			
A	10.1, -0.90	0.10, 0.18	—	16.3	0.27	—	14.4	13.1	
B	15.2	0.10	13.1	12.4	0.30	2.5	19.0	16.5	
E	—	—	6.1	0.28	—	9.1	—	—	
G ₁	—	—	—	-8.0	0.12	11.8	7.4	—	
G ₄	—	—	—	2.3	0.47	9.7	10.3	—	
G _{all}	3.8	...	3.1	...	4.2	...	9.5	10.4	10.1
H	—	—	—	10.7	0.64	5.2	—	—	
J ₁	8.4	0.03	—	—	—	—	—	—	
J ₂	—	—	4.2	2.70	7.5	0.98	7.2	—	
O	—	—	—	—	-1.5	0.49	3.8	-1.6	
R	—	—	—	—	8.6, 11.9	3.03	6.2	—	
South 1	13.6, 18.3	1.14, 1.54	—	—	—	8.5, 10.5	—	—	

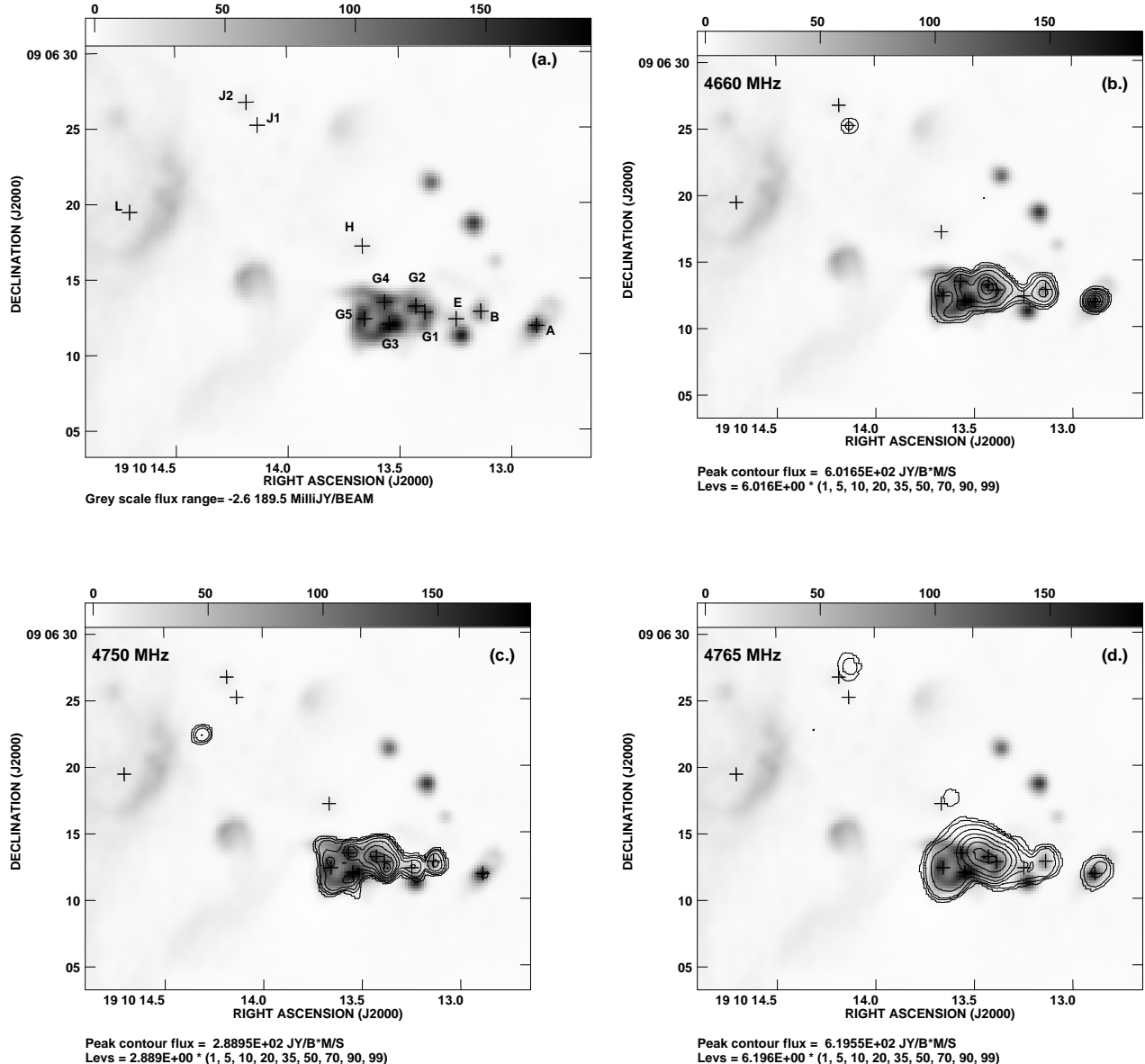


Figure 1. Comparison of 3.6-cm continuum emission from DMG with the velocity-integrated OH emission at 4660-, 4750-, and 4765-MHz in the extended OH region of W49A. (a) The 3.6-cm continuum emission from DMG is shown in grey scale. For the sources discussed in the text, the position for the continuum components provided by DMG is indicated by a cross and labelled. (L is a diffuse source of which only a bright arc is evident in this high resolution data. The position shown was determined from low resolution data and refers to the whole source.) The synthesised beam for this image is 0.8 arcsec. (b) The zeroth moment of the 4660-MHz OH emission on 2002 April 1 is represented by contours superimposed on the gray scale of the continuum. (c) The zeroth moment of the 4750-MHz OH emission on 2002 April 1 superimposed as in (b). In both (b) and (c), the OH image has been convolved to a circular beam with FWHM= 1.0 arcsec. (d) The zeroth moment of the 4765-MHz emission on 2002 June 1 represented by contours is superimposed on the gray scale of the continuum. The OH image has been convolved to a circular beam with FWHM= 2.0 arcsec. The contour levels are 1, 5 10, 20, 35, 50, 70, 90, and 99 per cent of the maximum in each OH image.

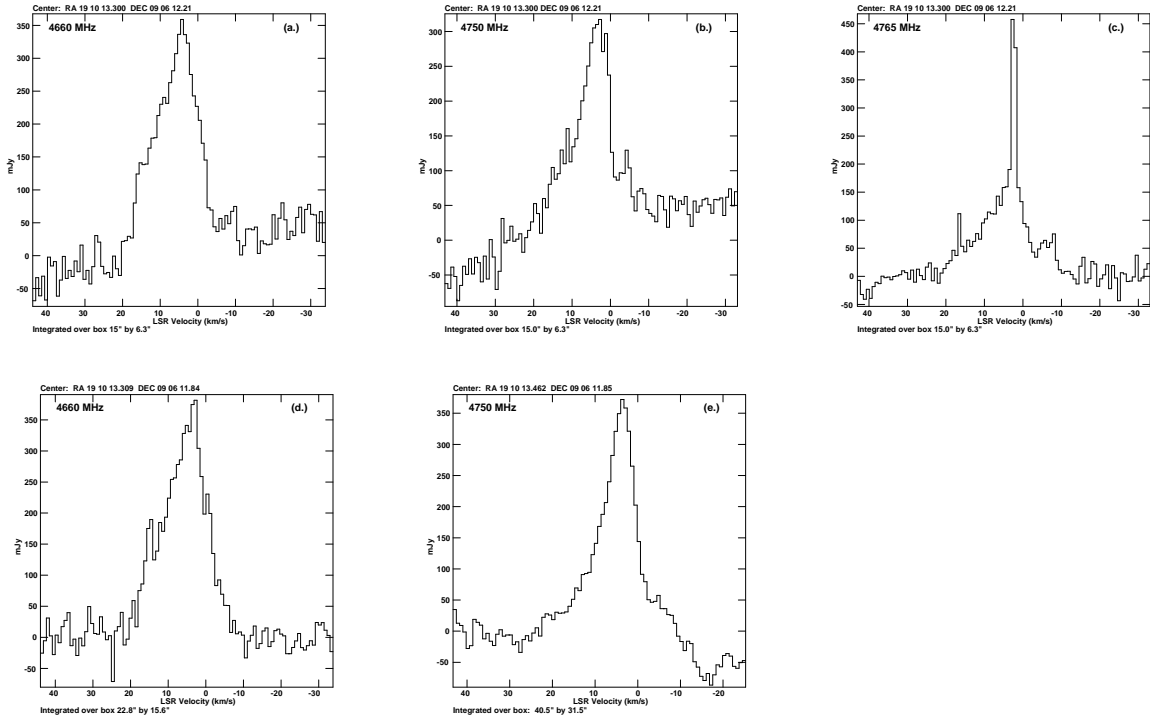


Figure 2. The 6-cm OH spectra integrated over regions covering sources G – A in the extended OH region. The dimensions of the regions are provided in Table 3. (a) The 4660-MHz line observed in 2002; (b) the 4750-MHz line observed in 2002; (c) the 4765-MHz line observed in 2002 (with narrow components near $V_{\text{LSR}}=2.3 \text{ km s}^{-1}$ and $V_{\text{LSR}}=16 \text{ km s}^{-1}$); (d) the 4660-MHz line observed in 2001; and (e) the 4750-MHz line observed in 2001. The baseline is truncated in (e) because of severe curvature at the low velocity end due to the lack of bandpass calibration at this date.

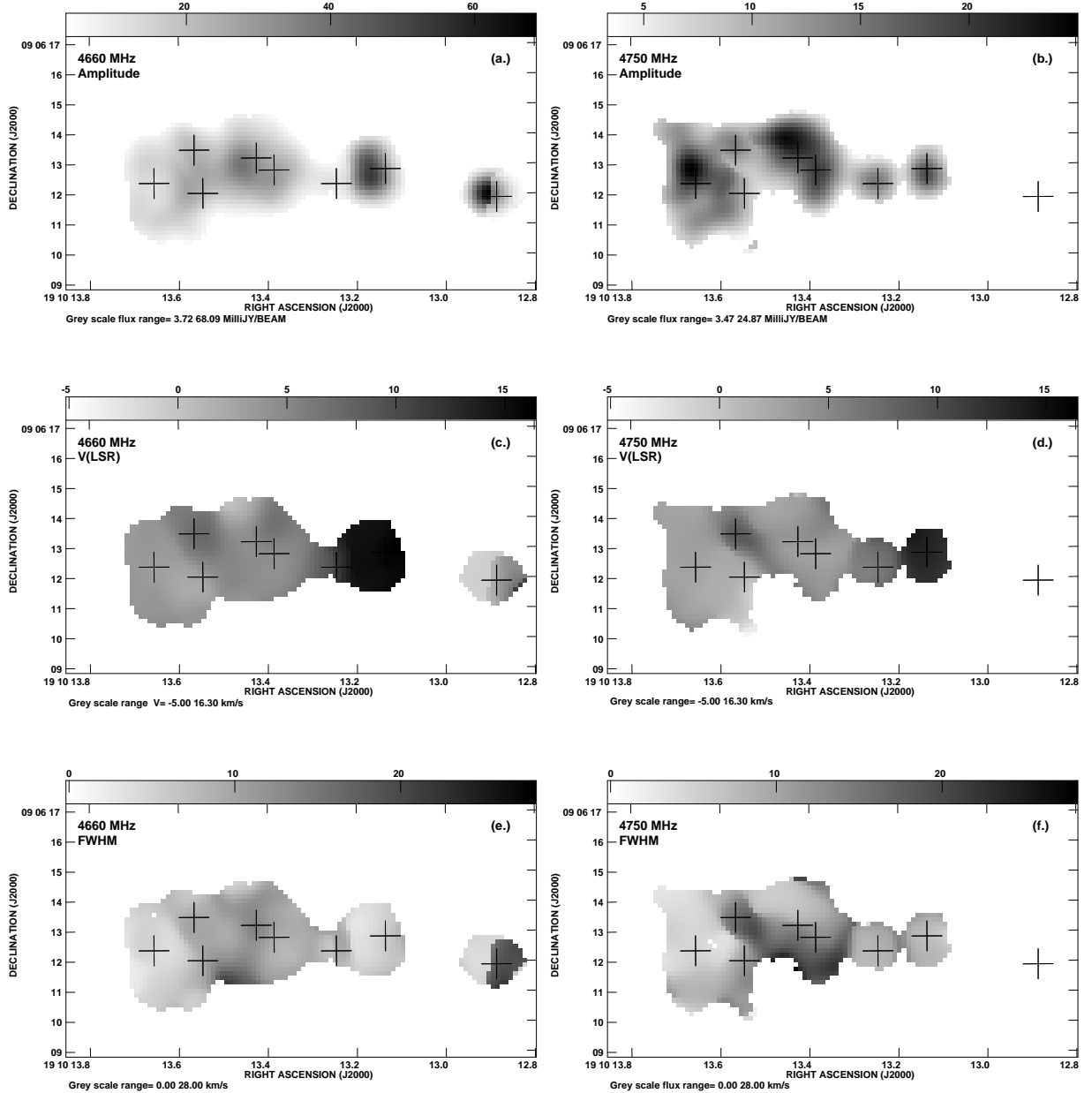


Figure 3. Images created from the results of Gaussian fits at each pixel in the source G – A region. The images were convolved to 1 arcsec resolution before fitting. Displayed are: the peak amplitude at 4660-MHz (a) and at 4750-MHz (b); the LSR velocity at 4660-MHz (c) and at 4750-MHz (d); and the FWHM of the spectrum at each point at 4660-MHz (e) and at 4750-MHz (f). For the identities of the crosses, see Fig. 1(a).

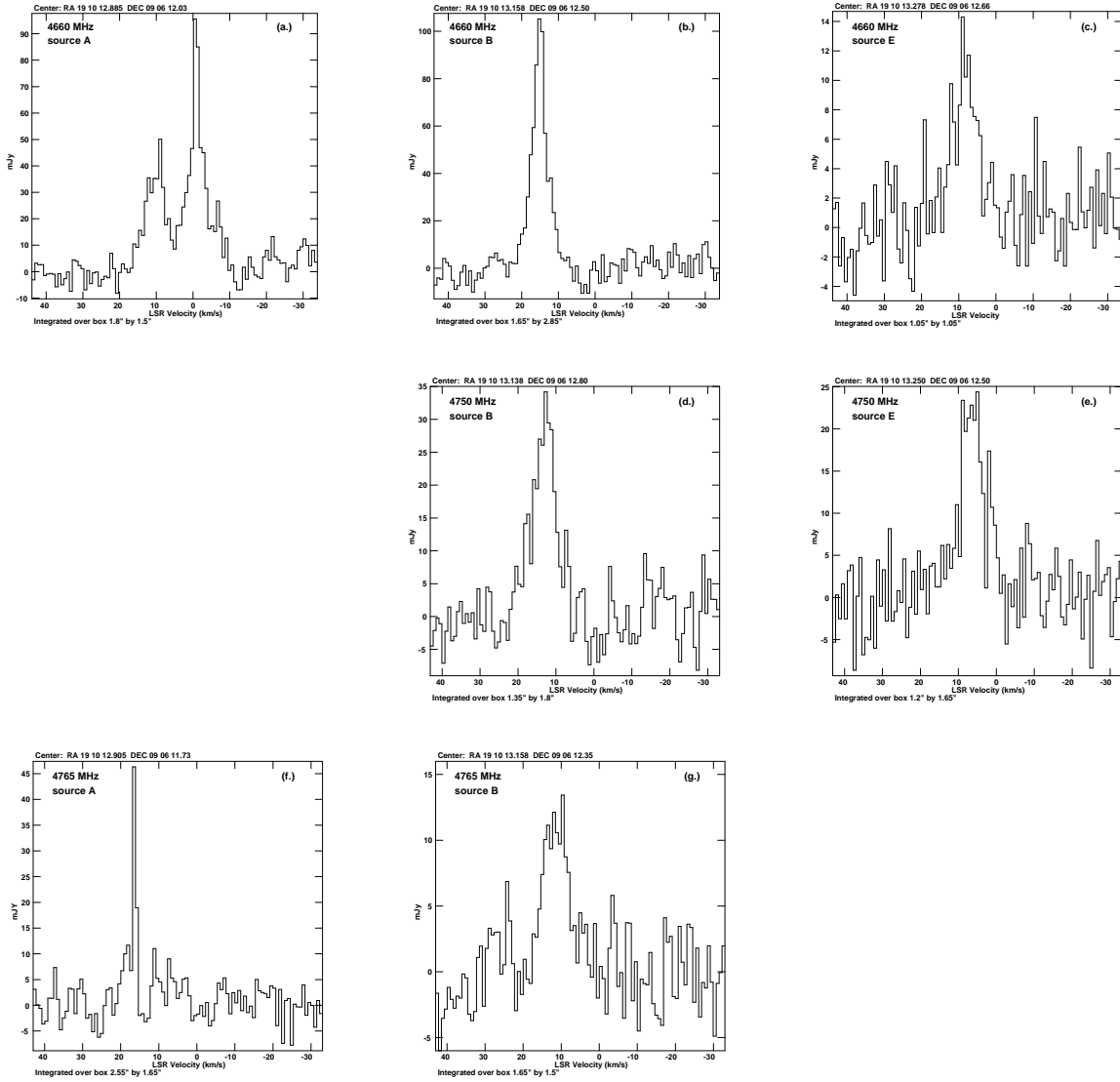


Figure 4. Spectra integrated over DMG components. (a) Source A at 4660-MHz; (b) source B at 4660-MHz; (c) Source E at 4660-MHz; (d) source B at 4750 MHz; (e) source E at 4750-MHz; (f) source A at 4765-MHz; (g) source B at 4765-MHz.

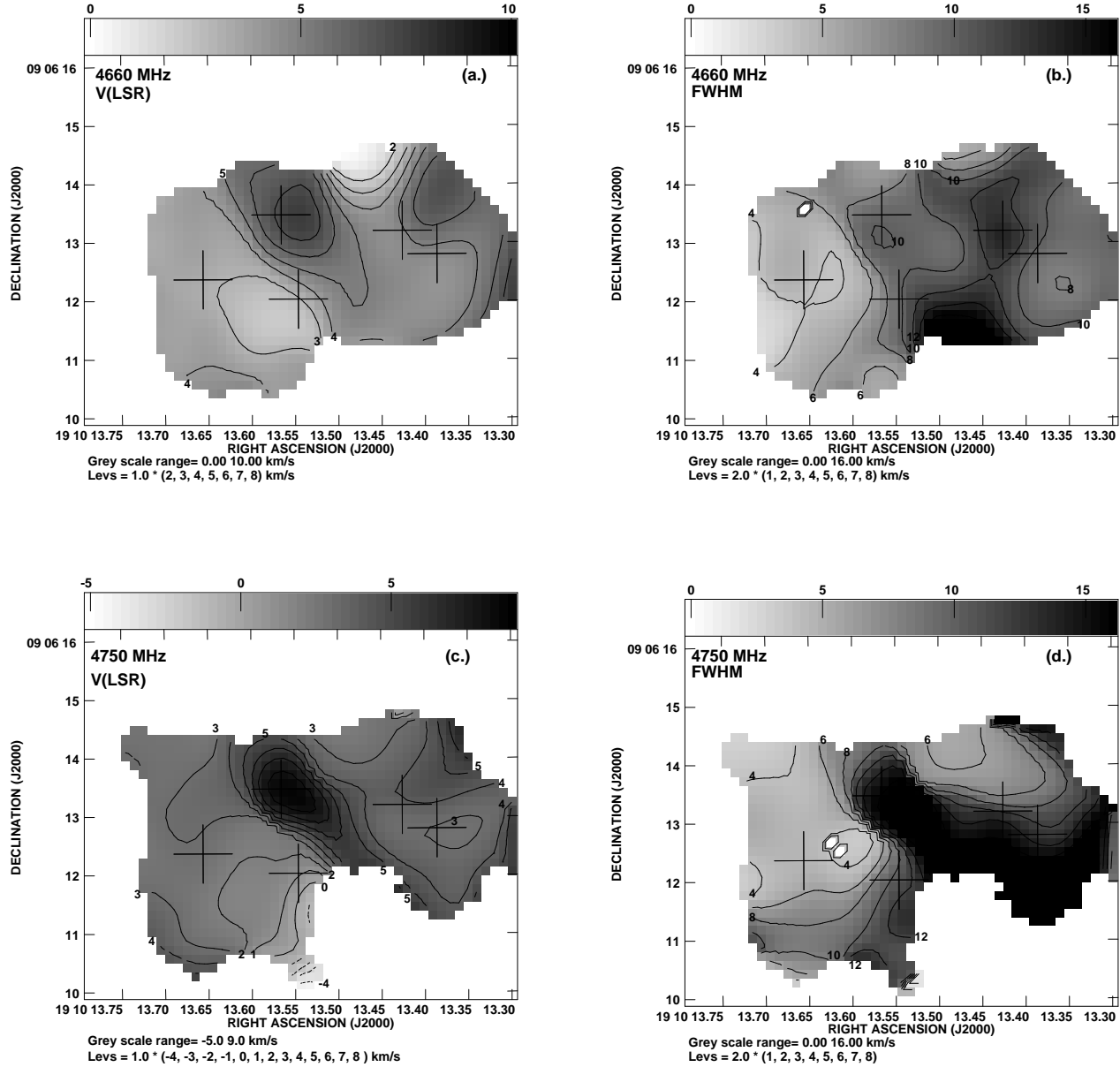


Figure 5. The V_{LSR} and FWHM variation within source G. (These panels are blowups of parts of Fig. 3 with contours superimposed.) (a) V_{LSR} at 4660-MHz; (b) FWHM at 4660-MHz; (c) V_{LSR} at 4750-MHz; (d) FWHM at 4750-MHz.

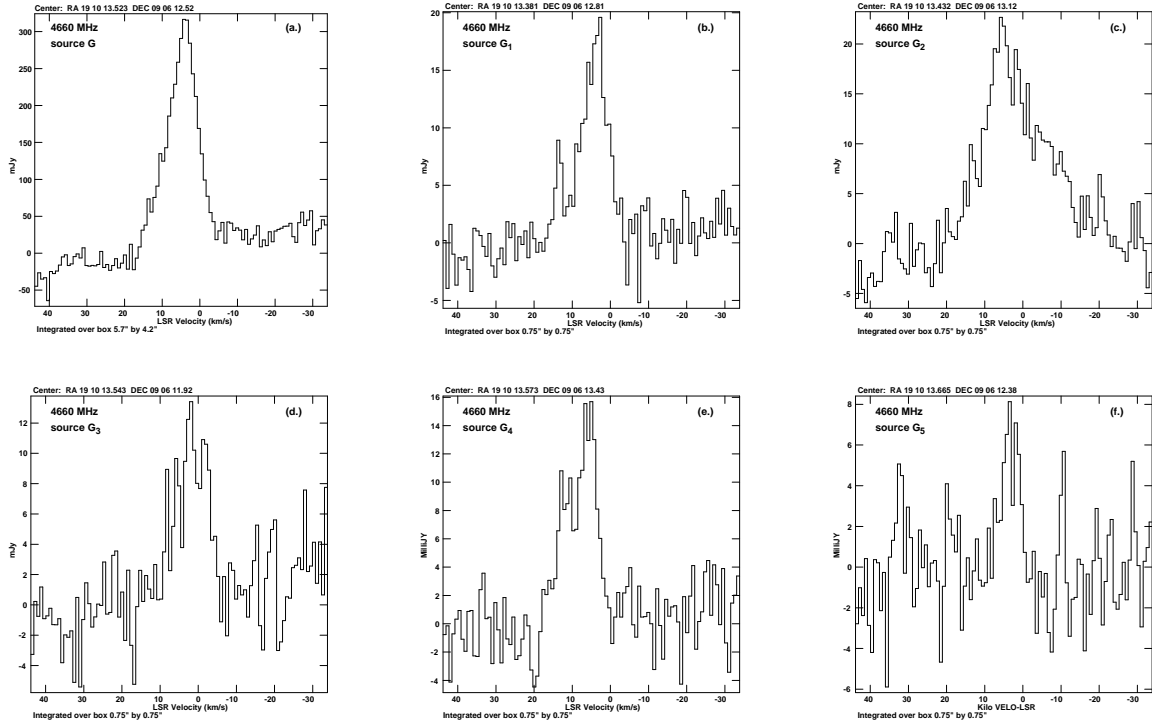


Figure 6. Spectra at 4660-MHz integrated over selected regions. (a) Integrated over the entire of Source G; (b) – (f) integrated over 0.75×0.75 arcsec 2 boxes at the positions of DMG components G₁ – G₅. Several spectra are distinctly non-Gaussian and suggest multiplicity. The spectrum of G₂ clearly contains multiple components.

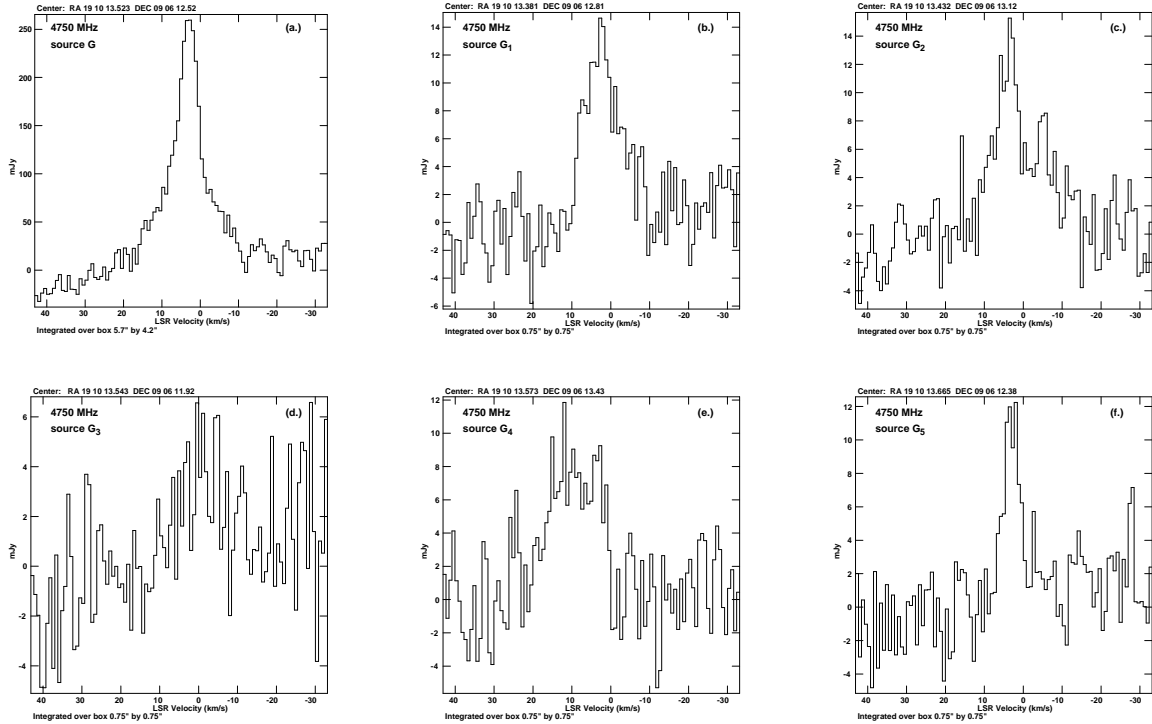


Figure 7. Spectra at 4750-MHz integrated over selected regions. (a) Integrated over the entire of Source G; (b) – (f) integrated over 0.75×0.75 arcsec 2 boxes at the positions of DMG components G₁ – G₅. Several spectra are distinctly non-Gaussian and suggest multiplicity.

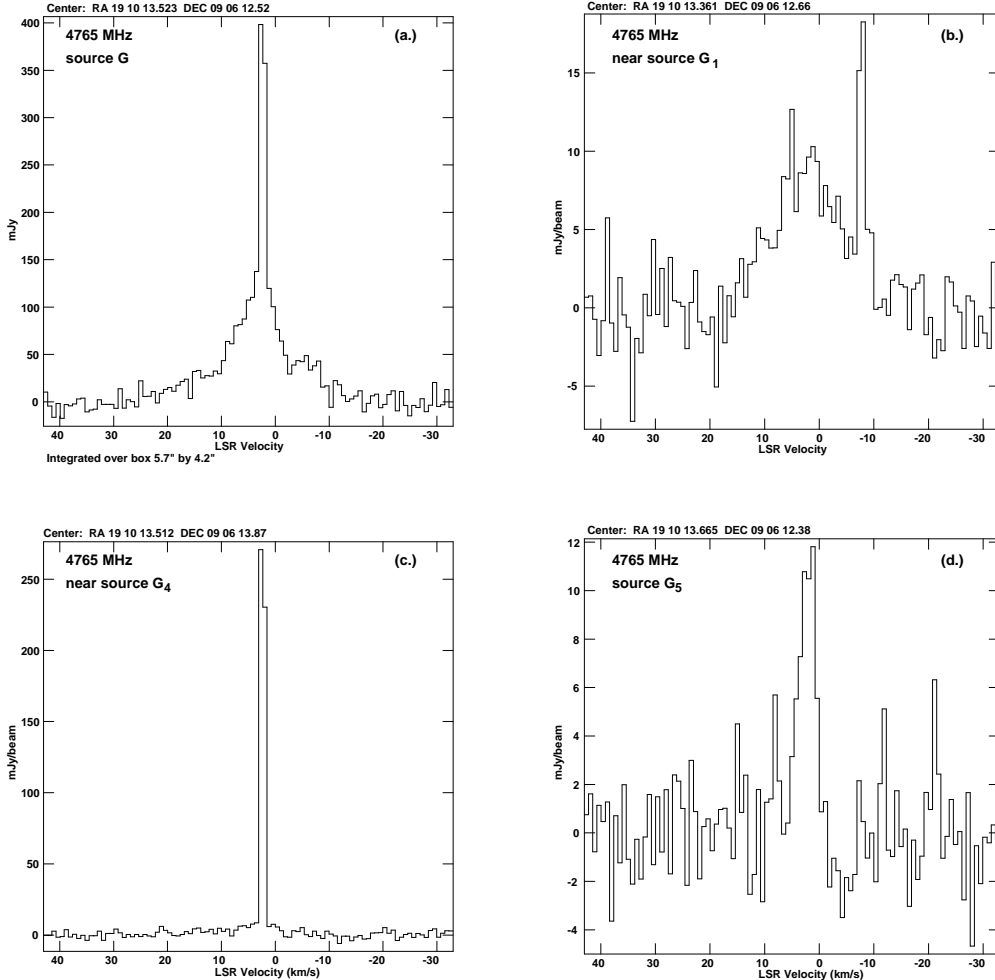


Figure 8. Spectra of source G at 4765-MHz. (a) Integrated over source G; (b) spectrum at the maximum near component G₁ (the narrow component at $V_{\text{LSR}} \sim 8 \text{ km s}^{-1}$ is the point-like component; the broad component is extended); (c) spectrum at the maximum near component G₄; (d) spectrum at the position of G₅.

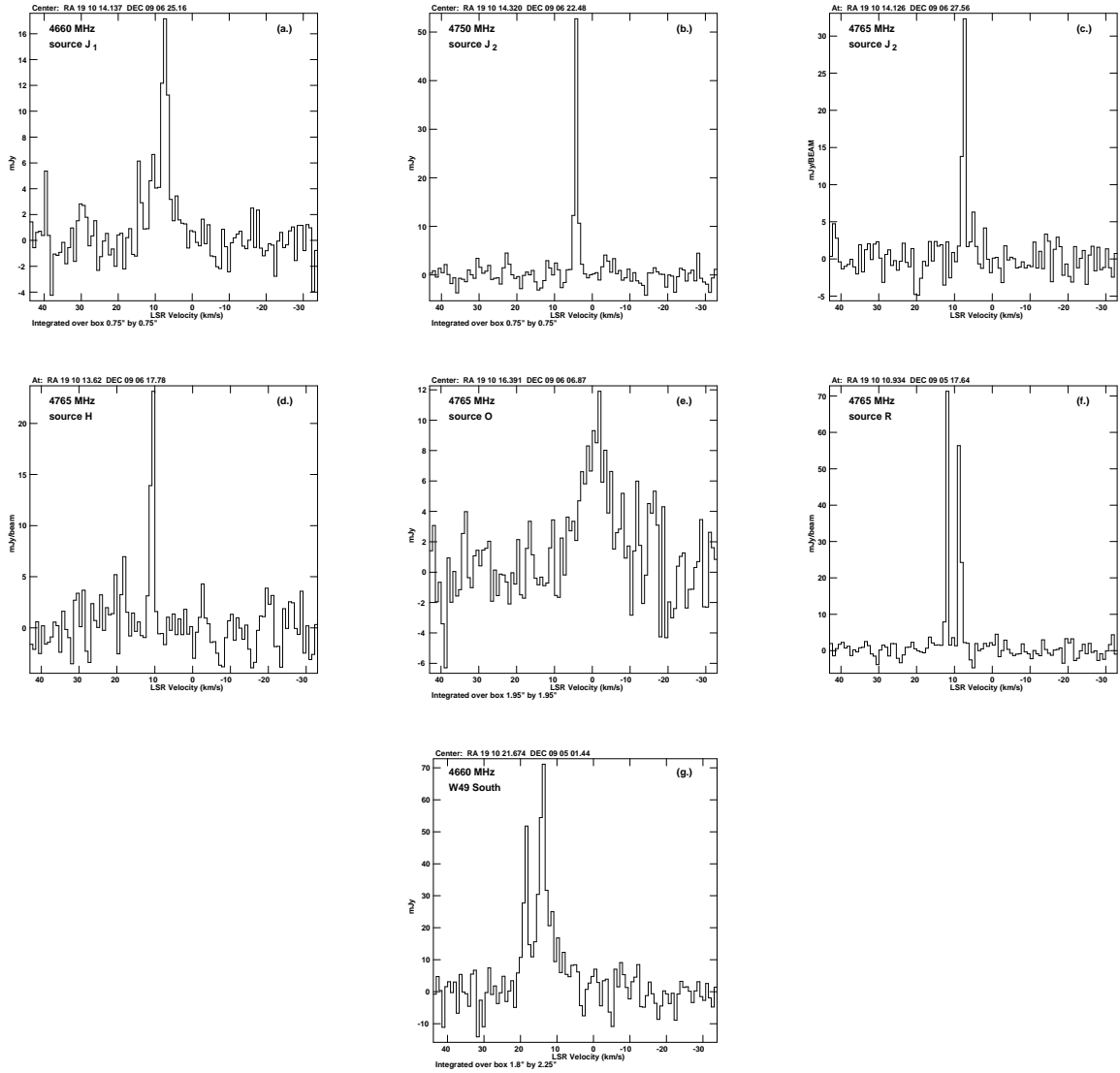


Figure 9. Spectra of sources outside of the extended OH region. (a) near source J₁ at 4660-MHz; (b) near source J₂ at 4750-MHz (this position could also be considered to be associated with the bright arc of source L); (c) near source J₂ at 4765-MHz. The positions of the spectra shown in (a) – (c) are separated by ~ 2 arcsec. (d) near source H at 4765-MHz; (e) near source O at 4765-MHz; (f) near R at 4765-MHz; (g) 4660-MHz source near W49 South.

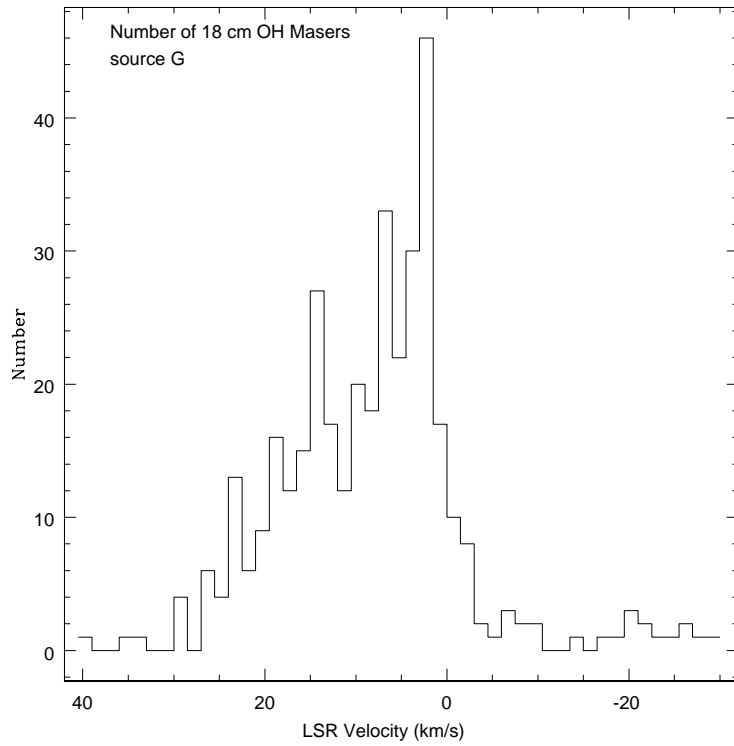
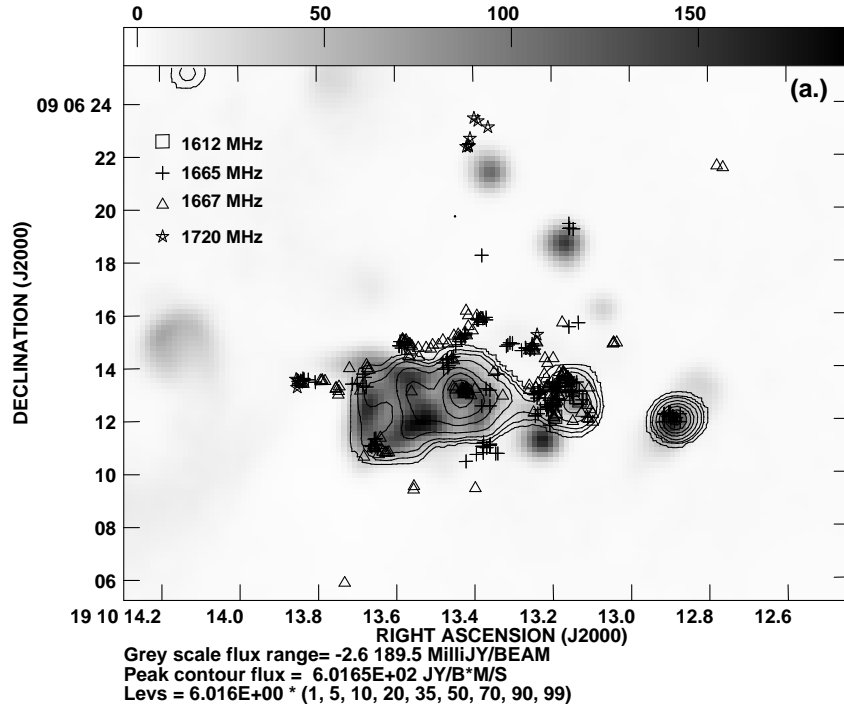


Figure 10. (a) Distribution of 18-cm masers from Gaume & Mutel (1987) superimposed on the 4660-MHz distribution (contours) and on the 3.6-cm continuum distribution (greyscale) as in Fig. 1. The symbols used to identify masers in the four 18-cm lines are shown on the left side of the figure. (b) A histogram of the velocity distribution of the 18-cm masers in this region. See text for details.